RSC Advances

ROYAL SOCIETY OF CHEMISTRY

www.rsc.org/advances

Journal Name

ARTICLE

Facile synthesis of free-standing Fe₂O₃/carbon nanotubes composite films as high-performance anodes for lithium-ion battery

Deming Yang,[ab] Shanshan Xu,[ab] Shuilang Dong,[ab] Jiachen Liu,[ab] Anran Guo,[ab] Xiao Yan, *[c] and Feng Hou*[ab]

Continuous Fe nanoparticles (NPs)/carbon nanotubes (CNTs) composite films have been fabricated along the CVD gas flow reaction using ferrocene as catalyst and ethanol as carbon precursor. The as-spun Fe NPs/CNTs films are converted to Fe₂O₃ NPs/CNTs films by an annealing process in the air at the temperature of 500 ºC. The as-prepared Fe₂O₃ NPs/CNTs films are still highly flexible. Scanning electron microscopy (SEM) and transmission electron microscopy observations reveal the Fe₂O₃ NPs are homogeneously bounded with CNT network. In addition, the flexible and conductive 3D CNTs networks endow the as-synthesized composite with increased electrical conductivity and mechanical stability. As a result, the as-synthesized flexible and transferrable composite films deliver an initial reversible capacity of 985.8 mA h g⁻¹ at current density of 30 mA g⁻¹, and maintain a high reversible capacity of 392.4 mA h g⁻¹ even at a current density up to 3 A g⁻¹. Meanwhile, Fe₂O₃ NPs/CNTs films exhibit excellent cycling performance with a reversible capacity of 375.5 mA h g⁻¹ after 800 cycles at the current density of 3 A g⁻¹.

Introduction

For the last few years, Li-ion batteries have been successfully applied in consumer electronic devices such as mobile phones and laptop computers. More recently the advent of electric of hybrid electric vehicles (HEV) and energy storage system for grid-scale applications has called for next generation Li-ion batteries with high energy density, high cycling stability and superb rate capability.[1, 2] However, the limited theoretical capacity of 372 mA h g⁻¹ of the commercial anode material of graphite cannot fully meet the requirement of high-energy density and high-power density. In this context, transition metal oxides (Fe₂O₃, NiO, Co₃O₄, etc.), have been extensively exploited as anode materials and exhibited remarkably high capacities (>700 mA h g⁻¹).[3-5] Among them, Fe₂O₃ has been investigated intensively for its high theoretical capacity (1007 mA h g⁻¹), low cost and environmental friendliness.[6-8] However the volume change of Fe₂O₃ during lithium ion insertion/extraction leads to poor cycling performance. In addition, the low electrical conductivity of pristine Fe₂O₃ makes it difficult to achieve high capacity at high charge/discharge rate.[4, 9]

Various approaches have been developed to tackle the above-mentioned drawbacks. One of the effective methods is to synthesize

nanostructured Fe₂O₃ materials with various desired morphologies, including nanoparticles, nanorods, nanotubes, and hollow nanostructures.[10-14] It is, by this means, expected to gain a shorter path for the transport of electrons and lithium ions and accommodate the mechanical strain of lithium ion insertion/extraction. Chen et al.[15] prepared Fe₂O₃ nanotubes with high initial discharge capacity of 1415 mA h g⁻¹, and remained 530 mA h g⁻¹ after 100 charge/discharge cycles. Xin et al.[16] assembled Fe₂O₃ xerogel from nanocrystalline particles (~5 nm) by hydrothermal method. The Fe₂O₃ xerogel displayed excellent rate capability (280 mA h g⁻¹ at 10 C). Yet simply decreasing the crystallite size to the nanoscale is not enough to overcome these problems since nanoparticles tend to agglomerate because of high surface energy.

Constructing hybrid electrodes with the combination of metal oxide and conductive carbon materials has been demonstrated to be a promising strategy to improve the electronic conductivity and stability of metal oxide during cycling.[17-21] Shao et al.[22] fabricated Fe₂O₃/carbon nanosprings by in-situ chemical precipitation and the subsequent heat treatment. These fabricated nanocomposites delivered a charge capability of 527.6 mA h g⁻¹ at 0.2 C with excellent cyclability (96.9% capacity retention after 50 cycles). Xia et al.[23] reported a Fe₂O₃/graphene foam hybrid materials which exhibited a specific capacity of 701 mA h g⁻¹ at current density of 50 mA g⁻¹. Even though the cycling performance of these iron oxide/carbon hybrids has been remarkably improved, the high rate performance of these materials still cannot meet the needs of the HEV and EVs. Moreover, in most conventional electrodes, the hybrid electrodes materials are directly mixed with a carbon additive and a binder to enhance electrical conductivity, which often results

[a.] School of Materials Science and Engineering, Tianjin University, Tianjin 300072, China
[b.] Key Laboratory of Advanced Ceramics and Machining Technology of Ministry of Education, Tianjin University, Tianjin 300072, China. E-mail: houf@tju.edu.cn
[c.] Guangdong Key Laboratory of Membrane Materials and Membrane Separation, Guangzhou Institute of Advanced Technology, Chinese Academy of Sciences, Guangzhou 511458, China
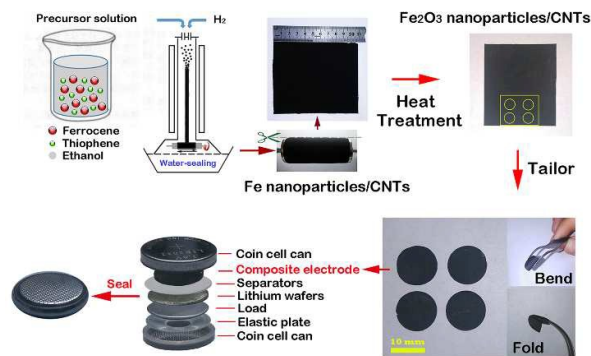
Figure 1. Preparation procedures of Fe_2O_3 nanoparticles/CNTs composite films and Coin cells.

in the deterioration of electrode (cracking, crumbling, or eventually pulverization) during cycling or high rate discharging.

Herein, we developed a facile and scalable synthesis strategy to fabricate free-standing Fe_2O_3 nanoparticles/CNTs composite films, in which Fe_2O_3 nanoparticles were homogeneously bounded in 3D porous carbon nanotube networks. The as-synthesized flexible and transferrable composite films can be used as electrode materials with no addition of carbon additive and binder, and exhibited high lithium storage capacity with superior cycling stability and high rate performance.

Experimental

Materials and synthesis

The Fe nanoparticles/CNTs composite film was continuously synthesized at 1100 °C in a vertical CVD system with water-sealing which we used before to prepare CNTs films.[24, 25] In contrast with the parameters of preparing CNTs films, we increased the concentration of ferrocene. And in this work we increased the amount of ferrocene from 1.7 wt.% to 3.2 wt.%, ethanol and thiophene were used as carbon source and growth promoter, respectively. When the system was heated to 1100 °C at a rate of 10 °C/min, the precursor solution were injected into the tube furnace at a rate of 8 mL/h using hydrogen as the carrier gas. Driven by H_2 at a flow rate of 800 sccm, the cylindrical Fe nanoparticles/CNTs film forming in the high-temperature zone moved downstream, and was eventually twined onto a spindle. And the time for twining is 40 min. After annealing at 500 °C for 1h under air, the Fe nanoparticles/CNTs composite films were converted to free-standing Fe_2O_3 nanoparticles/CNTs composite films. Detailed preparation procedures are illustrated in Fig. 1.

For comparison, Fe_2O_3 nanoparticles (Fe_2O_3 NPs) were prepared by thermal decomposition of ferrocene in air atmosphere at 500 °C, with which the commercial CNTs were mixed and then grinded for 1 h to get a uniform mixture of Fe_2O_3 NPs and CNTs, termed as Fe_2O_3/CNTs-mixed. And Fe_2O_3 NPs accounts for 63.2% of Fe_2O_3/CNTs-mixed by weight according to thermogravimetric analysis of Fe_2O_3 NPs/CNTs composite films.

Characterization

The crystalline phase of the prepared samples were identified by using X-ray diffraction (XRD, RIGAKU D Max 2500 V Pc) with a Cu Kα radiation. Raman spectroscopy was conducted on Renishaw Lab RAM HR800 with a diode laser with wavelength of 532 nm. Further, field emission scanning electron microscope (FE-SEM, JEOL, JSM-6700F) and transmission electron microscope (TEM, FEI, Tecnai G2F20) were applied to observe the morphologies and microstructures of the Fe_2O_3 nanoparticles/CNTs composite films. Thermogravimetric analysis (TGA, NETZSCH, STA 499C) was performed at a heating rate of 10 °C/min up to 1000 °C in air.

Electrochemical measurement

The electrochemical performance was evaluated using 2032 coin-type cells. A piece of wafer-shaped free-standing Fe_2O_3 NPs/CNTs composite film, which has a weight of around 2 mg and a diameter of 12 mm, was assigned as the negative electrode without any addition of carbon and binder. The conventional Fe_2O_3 and Fe_2O_3 NPs@CNTs electrodes were made by mixing the active materials with acetylene black and polyvinylidene fluoride respectively at a weight ratio of 8:1:1 and then vacuum dried at 120 °C for 12 h. Coin cells (CR2032) were fabricated using lithium metal as the counter electrode, Celgard 2400 as the separator, and LiPF6 (1M) dissolved in a mixture of ethylene carbonate/dimethyl carbonate (EC/DMC, 1:1 vol%) as the electrolyte. The assembly of the cell was conducted in an Ar-filled glovebox followed by an overnight aging treatment before the test. Cyclic voltammetry (CV) measurement was conducted at 0.1 mV/s within the range of 0.0-3.0 V on an electrochemical workstation (CH, CHI660D). The cycle life and rate capability of the cells were tested within a fixed voltage window of 0.005-3.000 V by using a battery test system (Neware, CT 3008W). Electrochemical impedance spectroscopy (EIS) measurements were carried out by using 5 mV AC amplitude over 100 kHz-0.01 Hz at the identical electrochemical workstation.
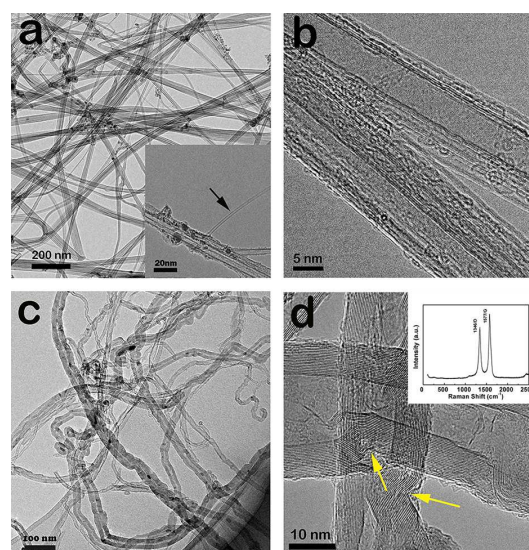

Figure 2. TEM images of CNTs films (a) and purchased CNTs (c); Magnified TEM images of CNTs films (b) and purchased CNTs (f), respectively.
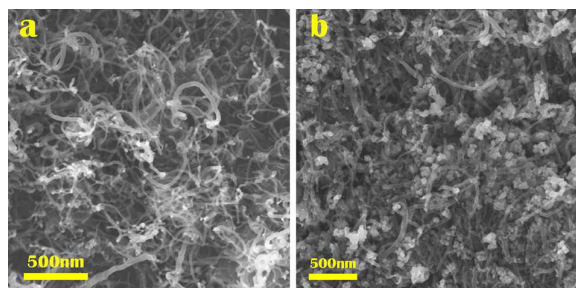
Figure 3. SEM images of commercial CNTs (a) and Fe$_2$O$_3$/CNTs-mixed (b)

Results and discussions

The micro-structures of CNTs films and purchased CNTs were first observed. The TEM images of CNTs films, shown in Fig. 2a and b, indicate that CNTs films synthesized using a novel floating catalyst chemical vapor deposition method in our group are composed of small amounts of single-walled CNTs (shown by black arrow in the inset of Fig. 2a) and straight long interconnected CNT bundles piled up from several multiwall CNTs with large aspect ratio and few defects.

These features differ significantly from purchased CNTs. According to the information provided by the manufactures, the diameter, length and specific surface area of the commercial CNTs are 20-30 nm, 5-15 μm and 150-210 m^{2}g^{-1}, respectively. As shown in Fig. 2c and Fig. 3a, the commercial CNTs are curly with some agglomerations and have a smaller aspect ratio. Thus the short and curly CNTs cannot construct a uniform and continuous 3D network when composited with metal oxide[26, 27] as shown Fig. 3b. And the
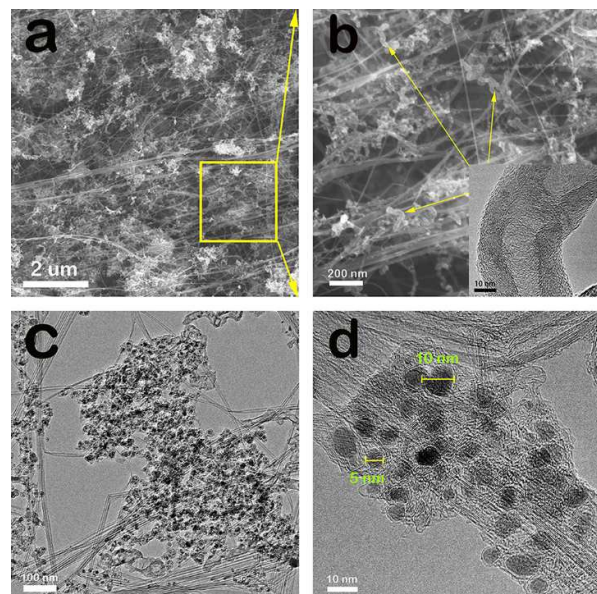

Figure 4. FE-SEM images of Fe NPs/CNTs composite films (a) and (b); TEM images (c) and Magnified TEM images (d) of Fe NPs/CNTs composite films.
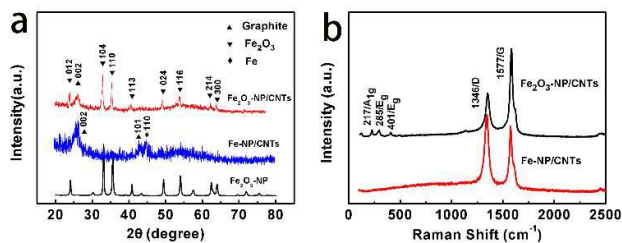

Figure 5. (a) XRD patterns of the as-synthesized Fe$_2$O$_3$ NPs/CNTs composite film, Fe NPs/CNTs and pure Fe$_2$O$_3$ NPs. (b) Raman spectra of Fe NPs/CNTs and Fe$_2$O$_3$ NPs/CNTs.

Raman spectra of commercial CNTs, as demonstrated by inset in Fig. 2d, further insights into the structure. The peak intensity ratio between D-bands and G-band (I_D/I_G) was calculated 0.96, indicating low graphitic crystallinity of carbon nanotubes (shown by arrows in Fig. 2d). Meanwhile, small amounts of spherical catalyst particles (diameter in 3～8 nm range) encapsulated by carbon shells usually adhere to the CNTs bundles in CNTs films, as demonstrated by inset in Fig. 2a. It is worth noting that the catalyst particles will be oxidized into iron oxide (Fe$_2$O$_3$) when calcinated in air.

Fe NPs/CNTs composite films were obtained when ferrocene was increased from 1.7 wt.% to 3.2 wt.%. As shown in Fig. 3a and b, significant change on microstructure occured with the increase of ferrocene. Comparing to pristine CNTs films, the continuous 3D CNTs network composed of CNT bundles and small amounts of SWNTs is decorated uniformly by a large amount of catalyst nanoparticles. High-magnification TEM image (Fig. 4d) of Fe NPs/CNTs composite films clearly reveal that the Fe nanoparticles disperse uniformly in CNTs network. As clearly shown in the comparison, excessive high concentration of ferrocene tends to form inactivated nanoparticles encapsulated by carbon shells. The formation of large number of catalyst particles when increasing catalyst concentration has been reported by literature research for synthesis of SWCNTs.[28, 29] Meanwhile, there is also a slight increase in the particle size as shown in Fig. 4d. The size of catalyst particles for Fe NPs/CNTs is about 5~10 nm, slightly larger than that for CNTs. The aggregation of catalyst atoms increases with ferrocene concentration, which leads to larger particles.[30, 31] It should be noted that a handful of curved and short CNTs were observed as shown in Fig. 4b. The inset in Fig. 4b indicates that the curved and short CNTs are defective and have poor crystallinity. This should result from the excess catalyst particles, which bring in several factors including vapor pressure-driven movement of metal catalyst,[32] unstable gas-flow, and turbulence of carbon source gas,[33] resulting in lattice distortion of CNTs.

After careful annealing in the air, the Fe NPs/CNTs composite films was oxidized and converted to Fe$_2$O$_3$ NPs/CNTs composite films, which was confirmed by X-ray diffraction (XRD) analysis shown in Fig. 5a. It can be found that Fe nanoparticles/CNTs composite films exhibit two distinct diffraction peaks at 26.3° and 43.0°, corresponding to (002) and (101) crystal planes of CNTs respectively. The peaks at 44.8° for Fe nanoparticles disappeared after air annealing, while the characteristic diffraction peaks

at 26.3° and 43.0°, corresponding to (002) and (101) crystal planes of CNTs respectively. The peaks at 44.8° for Fe nanoparticles disappeared after air annealing, while the characteristic diffraction peaks emerged at 24.1°, 33.1°, 35.6°, 40.8°, 49.5°, 54.1°, 62.4°, and 64.0°, matched well with the (012), (104), (110), (113), (024), (116), (214), (300) crystal planes of Fe_2O_3 (α- Fe_2O_3, JCPDS Card No. 33-0664). This indicated the conversion from Fe NPs/CNTs to the targeted sample (Fe_2O_3 NPs/CNTs composite film) by air annealing.

Raman spectra were employed to obtain further insights into the structural change related to the air annealing process. The data were presented in Fig. 5b. After annealing, the typical Raman scattering peaks for Fe_2O_3 at 217, 285 and 401 cm^{-1} were indentified, further confirming that the Fe NPs/CNTs were oxidized and converted to Fe_2O_3 NPs/CNTs. Additionally, the Raman spectra for the Fe NPs/CNTs and Fe_2O_3 the NPs/CNTs samples reveals two distinguishable peaks at about 1346 cm^{-1} and 1577 cm^{-1}, characteristic features of the disordered (D) and graphitic (G) bands from CNTs, respectively. The peak intensity ratio between D-band and G-band (I_D/I_G) generally provides a useful index for comparing the degree of crystallinity of various carbon materials. The smaller the ratio of I_D/I_G, the higher the degree of ordering in the carbon material. The I_D/I_G ratio of Fe NPs/CNTs was calculated to be 1.15 while reduced to 0.39 after annealing, indicating high graphitic crystallinity of carbon nanotubes in the Fe_2O_3 NPs/CNTs composite, which should be beneficial to achieve an electronic and ionic conduction highway and lowering the internal electrode resistance.

SEM (Fig. 6a) and TEM (Fig. 6c) images show that both the carbon shells and short curved CNTs disappeared after air annealing. While the porous 3D CNTs network of the Fe NPs/CNTs composite films were well-maintained in the Fe_2O_3 NPs/CNTs composite films, which is in agreement with the Raman spectra. The skeleton texture
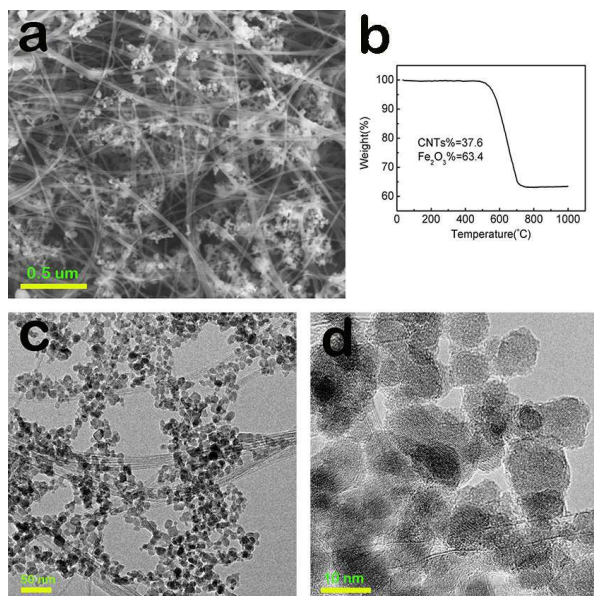

Figure 6. (a) FE-SEM images and (c) TEM image of Fe_2O_3 NPs/CNTs composite films; (b) TGA profile of Fe_2O_3 NPs/CNTs composite films; (d) magnified TEM images of Fe_2O_3 NPs/CNTs composite films.
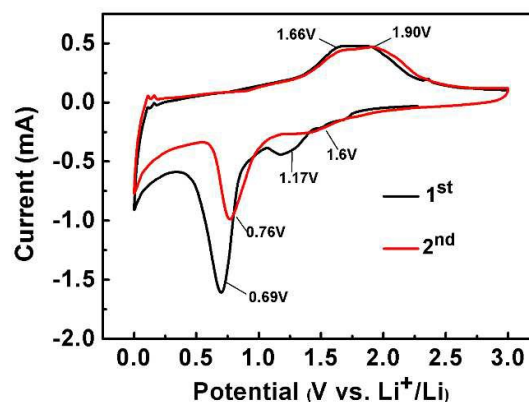

Figure 7. CV curves of Fe_2O_3 NPs/CNTs composite films obtained at a voltage range of 0.01 to 3.0 V (vs Li^+/Li) and potential scan rate of 0.1 mV/s.

constructed by straight long interconnected CNT bundles endowed the Fe_2O_3 NPs/CNTs composite films with high flexibility. As shown in Fig. 1, wafers tailored from Fe_2O_3 NPs/CNTs composite films are flexible, foldable and can be directly used as electrodes in lithium-ion battery (without any binder and carbon additive). Compared with other carbon-based matrices,[20, 21, 34, 35] the porous, continuous and conductive 3D CNTs network constructed by well-crystallized CNTs can greatly facilitate the diffusion of both electrons and lithium ions. High-magnification TEM images (Fig. 6d) of Fe_2O_3 NPs/CNTs composite films clearly reveal that the Fe_2O_3 NPs are highly crystallized. Moreover, the Fe_2O_3 NPs size (5-10 nm) were smaller than those in literature reports.[36, 37] Thermogravimetric analysis (TGA), carried out at a heating rate of 10 °C/min in air, was used to determine the chemical composition of the Fe_2O_3 NPs/CNTs composite films. The sample was heated up to 1000 °C to guarantee complete CNTs oxidation to CO_2. The fraction of Fe_2O_3 is calculated to be 63.4% by weight.

The electrochemical behaviors of Fe_2O_3 NPs/CNTs composite films were tested by cyclic voltammogram (CV, Fig. 7) for the initial two Li-ion insertion/extraction cycles with a scan rate of 0.1 mV/s. Three main cathodic peaks at 1.6, 1.17 and 0.69 V can be observed in the initial negative scan, corresponding to three lithiation steps with different iron states.[38, 39] The first small peak reflects the formation of Li-intercalated hexagonal phase (α-$Li_xFe_2O_3$). The second peak is relevant to the formation of Li-intercalated cubic phase ($Li_2Fe_2O_3$). The sharp peak at 0.69 V shows reduction of Fe^{2+} to Fe^0 and decomposition of electrolyte which results in the formation of solid electrolyte interface (SEI)[6]. The positive scan shows a broad peak at 1.66-1.90 V, indicating two steps of oxidation reaction of Fe (from Fe^0 to Fe^{2+}, then from Fe^{2+} to Fe^{3+}, respectively). As shown in Figure 7, the initial peaks at 1.17 V and 1.6 V disappear in the second cycle as a result of irreversible formation of α-$Li_xFe_2O_3$ and irreversible phase transition from α-$Li_xFe_2O_3$ to cubic $Li_2Fe_2O_3$. And the peak intensity at 0.76 V drops significantly in the second cycle, indicating the occurrence of some irreversible reactions with formation of SEI film. The reproducibility
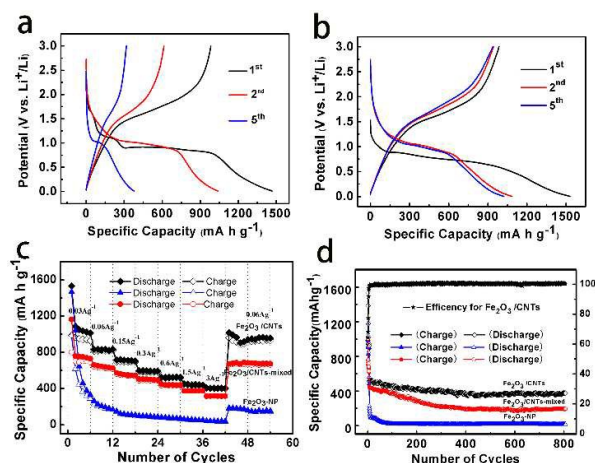
Figure 8. Galvanostatic discharge/charge curves of (a) pristine Fe_2O_3 NPs and (b) Fe_2O_3 NPs/CNTs composite films for the initial 5 cycles at 30 mA g^{-1}. (c) Charge/discharge capacity of Fe_2O_3 NPs/CNTs composite films, pristine Fe_2O_3 NPs and Fe_2O_3/CNTs-mixed at a various current densities between 30 mA g^{-1} and 3 A g^{-1}. (d) Cycling performance of Fe_2O_3 NPs/CNTs composite films, pristine Fe_2O_3 NPs and Fe_2O_3/CNTs-mixed measured at 3 A g^{-1} for 800 cycles.

with cathodic and anodic peak pair at 0.76 V and 1.66-1.90 V indicate the reversible conversion between Fe^{2+} and Fe^0.

Motivated by the unique structure and morphology of Fe_2O_3 NPs/CNTs composite films, we have evaluated the electrochemical lithium storage properties of as-synthesized composite for their potential use as an anode material for LIBs. Fig. 8b shows representative discharge/charge voltage profiles of this material at a current density of 30 mA g^{-1} within a cut-off voltage window of 0.01-3.0 V. It can be seen that the sample delivers a very high lithium storage capacity of 1532.3 mA h g^{-1} and a relative low reversible capacity of 985.8 mA h g^{-1}, leading to an initial Coulombic efficiency (CE) of around 64.3% in the first cycle. The irreversible capacity loss should result from the irreversible processes including the formation of SEI and electrolyte decomposition. The discharge voltage plateau at ~0.7 V in the first cycle is different from the followed cycles at ~1.0 V. This characteristic also agrees well with the CV results, further indicating the irreversible reactions occurred in the first cycle. And the discharge/charge profiles of the next four cycles are almost identical to each other with the CE rising to 92%, which is higher than that of pristine Fe_2O_3 NPs (84% for the fifth cycle). It should be noted that the charge capacities for the fifth cycle are 939.0 mA h g^{-1} with 95% retention, while the capacity of pristine Fe_2O_3 NPs showed a continuous decay throughout the first five cycles (only 32% retention after five cycles). Such excellent CE and stabilized capacity of Fe_2O_3 NPs/CNTs composite films benefits mainly from the porous 3D CNTs network, which efficiently prevents agglomeration of Fe_2O_3 NPs during cycling, thus making Fe_2O_3 NPs fully accessible to lithium ions in the electrolyte. On the other hand, the porous 3D CNTs network acts as confining buffer, alleviating

severe volume change of Fe_2O_3 during Li-ion insertion/extraction cycling.

Fig. 8c shows a comparison on specific capacity at different current densities between Fe_2O_3 NPs/CNTs composite films, pure Fe_2O_3 NPs and Fe_2O_3/CNTs/mixed. The rate capability of Fe_2O_3 NPs/CNTs composite films drastically outperforms that of pure Fe_2O_3 NPs and Fe_2O_3/CNTs-mixed. Even at the current density of 3 A g^{-1}, the Fe_2O_3 NPs/CNTs composite films can deliver a capacity of 392.4 mA h g^{-1}. Whereas pure Fe_2O_3 NPs exhibits almost no capacity (36.9 mA h g^{-1}) and the capacity of Fe_2O_3/CNTs-mixed is 314.9 mA h g^{-1} when the current density is 3 A g^{-1}. After the rate tests for 48 cycles, the capacity of Fe_2O_3 NPs/CNTs composite films can be recovered to 932.3 mA h g^{-1}, while pure Fe_2O_3 NPs and Fe_2O_3/CNTs-mixed only restore to 144.9 mA h g^{-1} and 660.1 mA h g^{-1} respectively when the current density returns to 60 mA g^{-1}, indicating that Fe_2O_3 NPs/CNTs composite films have much better capacity retention than pure Fe_2O_3 NPs and Fe_2O_3/CNTs-mixed. The increase in capacity when the current density returns to 60 mA g^{-1} for Fe_2O_3 NPs/CNTs composite films can be attributed to the reversible formation of organic polymeric/gel-like layer by electrolyte decomposition at low potential, which can coat around the active materials to ensure the mechanical cohesion and deliver excess capacity.[4, 40]

To further highlight the superiority of the unique Fe_2O_3 NPs/CNTs composite films at high rate for anode materials of LIBs, we tested the cycle performance of Fe_2O_3 NPs/CNTs composite films, pure Fe_2O_3 NPs and Fe_2O_3/CNTs-mixed. As shown in Fig. 8d, in the first 100 cycles, the capacity decreases slightly for both Fe_2O_3 NPs/CNTs composite films and Fe_2O_3/CNTs-mixed. In the contrary, there is a rapid decay for the capacity of pure Fe_2O_3 NPs. During the following cycles, the Fe_2O_3 NPs/CNTs composite films demonstrated enhanced cycling stability and higher reversible specific capacity compared with pure Fe_2O_3 NPs and Fe_2O_3/CNTs-mixed. After 800 cycles at the current density of 3 A g^{-1}, the reversible capacity of Fe_2O_3 NPs/CNTs composite films is as high as 375.5 mA h g^{-1}, better than 13.9 mA h g^{-1} of pure Fe_2O_3 NPs and 190.0 mA h g^{-1} of Fe_2O_3/CNTs-mixed. The coulombic efficiency of
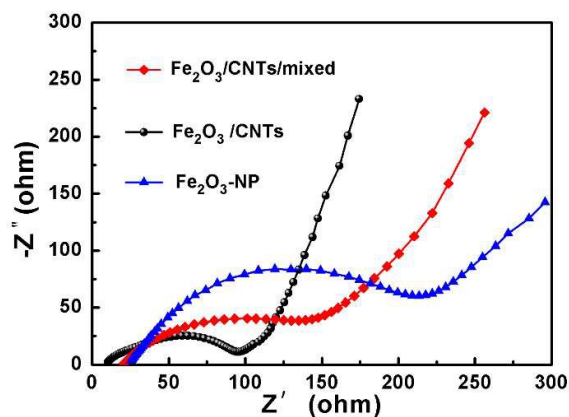

Figure 9. Nyquist plots of the Fe_2O_3 NPs/CNTs composite films, pristine Fe_2O_3 NPs and Fe_2O_3/CNTs-mixed at fresh coin cells over the frequency range from 100 kHz to 0.01 Hz.
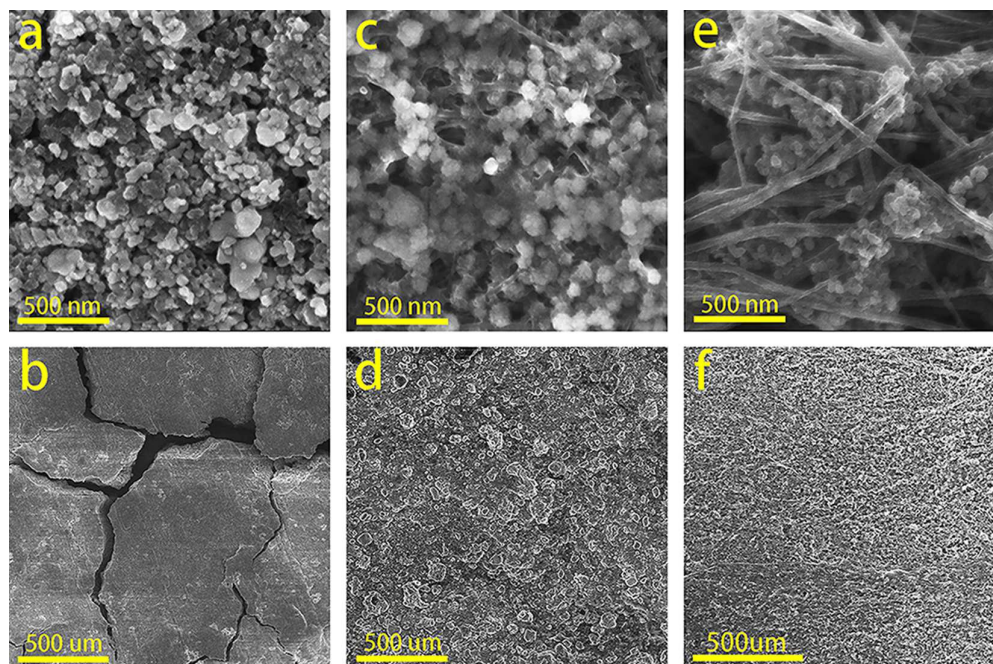
Figure 10. SEM images of cycled electrodes after cycling for (a, b) Fe_2O_3 NPs, (c, d) Fe_2O_3/CNTs-mixed, and (e, f) Fe_2O_3 NPs/CNTs composite films.

Fe_2O_3/CNTs composite films rapidly increases from 64% for the first cycle to about 99% after three cycles and remains nearly 100% thereafter, suggests a facile lithium insertion/extraction associated with efficient transport of ions and electrons in the porous 3D CNT networks. The drastically enhanced cycling stability and capacity retention, as we expected, is attributed to the continuous and tough CNTs network which strengthens the structural integrity of Fe_2O_3 NPs/CNTs composite films and greatly facilitates the diffusion of both electrons and lithium ions.[41, 42] Furthermore, low dimensional Fe_2O_3 nanoparticles (5-10 nm) with increased surface area improve contact between the solid and the electrolyte, shorten the route for lithium diffusion, and minimize the effects of volume change,[43, 44] resulting in more stable and efficient performance at high rate compared to large Fe_2O_3 nanoparticles.

The EIS measurements were performed for better understanding of the electrochemical performance. The corresponding Nyquist plots of Fe_2O_3 NPs/CNTs composite films, pure Fe_2O_3 NPs and Fe_2O_3/CNTs-mixed are given in Fig. 9. Clearly, all the Nyquist plots for three materials consist of one compressed semicircle at the high frequency region, indicative of the charge-transfer resistance (R_{ct}) in the electrode reaction, and an inclined line at the low frequency region which represents the Warburg impedance (Z_W) related to the diffusion of Li ions in the electrode materials.[45, 46] Both R_{ct} and Z_W of Fe_2O_3 NPs/CNTs composite films are substantially reduced when compared to pure Fe_2O_3 NPs and Fe_2O_3/CNTs-mixed as shown in Fig. 9. Convincingly, the continuous conductive CNTs network in the Fe_2O_3 NPs/CNTs composite films endow the as-synthesized composite with favorable electronic and ionic conduction highway and lower the internal electrode resistance. This evidence further supports the superiority of Fe_2O_3 NPs/CNTs composite films as the anode materials for LIBs.

The SEM images of cycled electrodes for Fe_2O_3 NPs, Fe_2O_3/CNTs-mixed, and Fe_2O_3 NPs/CNTs composite films are given

Figure 11. Strength test of Fe_2O_3 /CNTs-a, b and c.

in Fig. 10. As Fig. 10a shown, clear agglomeration appeared after cycling for Fe_2O_3 NPs electrode, and the electrode cracked seriously (Fig. 10b) resulting in a poor rate and cycle performance. From Fig. 10c and d we can see that the addition of commercial CNTs decrease the agglomeration and avoid the fragmentation during cycling. While, blocks still appeared on the surface of electrode, which may give rise to the rapid decline of capacity during the first 400 cycles (Fig. 8d). After cycling, the morphology of Fe_2O_3 NPs/CNTs composite films is well maintained with porous structures and Fe_2O_3 NPs is still bounded by the continuous and flexible CNTs networks, eliminating the agglomeration of Fe_2O_3 and crack of electrodes. As a result, Fe_2O_3 NPs/CNTs composite films have an outstanding rate and cycle performance compared with Fe_2O_3 NPs and Fe_2O_3/CNTs-mixed.

As we know that the physical properties such as thickness and mechanical property of the films will greatly affect their electrochemical performance when using as free-standing lithium ion battery anodes[47]. Composite films with various thicknesses were obtained by adjusting the winding time as 20 min, 40 min and 60 min. After air annealing at 500 °C for 1h, the corresponding Fe_2O_3 nanoparticles/CNTs films were termed as Fe_2O_3/CNTs-a, b and c. The thickness of Fe_2O_3/CNTs-a, b and c is 0.01 mm, 0.02 mm and 0.04 mm, respectively. Although at this stage we have difficulty testing the mechanical property of Fe_2O_3 NP/CNTs composite films, we managed to determine the strength of the composite films in a vivid method as shown in Fig. 11. The composite films were cut into rectangular pieces (1.5 cm×5 cm) and loaded with various standard weights. Fe_2O_3/CNTs-a can bear the weight of 10 grams. And with the increase of thickness, the Fe_2O_3/CNTs-b and c can bear the weight of 50 grams and 100 grams.

The rate performances of Fe_2O_3/CNTs electrodes with different thicknesses at various charge rates is shown in Fig. 12. Fe_2O_3/CNTs-a delivers a capacity of 823.4 mA h g^{-1} when first cycled at 0.3 A g^{-1}, which is higher than that of Fe_2O_3/CNTs-b and c. Even at high rates of 1.5 A g^{-1} and 3 A g^{-1}, the reversible capacities still retain approximately 555.2 mA h g^{-1} and 480.3 mA h g^{-1}, respectively. The super rate performance of Fe_2O_3/CNTs-a is attributed to its much shorter electronic conductive paths calculated from current collector to the furthest active sites for energy storage[48]. Both Fe_2O_3/CNTs-b and c exhibit superior cycling stability with a very slow fade after 100 cycles at the rate of 1.5 A g^{-1}. On the contrary, Fe_2O_3/CNTs-a shows a great decrease from 567.4 mA h g^{-1} to 473.3 mA h g^{-1} after 100 cycles, yet still higher than those of Fe_2O_3/CNTs-b and c. The poor cycling performance of Fe_2O_3/CNTs-a should arise from less active Fe_2O_3 nanoparticles[49] and lower strength compared with Fe_2O_3/CNTs-b and c. Therefore, we speculate that thinner Fe_2O_3/CNTs composite film can present higher capacity and rate capability. However, Fe_2O_3/CNTs composite films thinner than 20 μm may have poor practical application because of their low strength and few active materials.

Conclusions

In summary, free-standing Fe_2O_3-NPs/CNTs composite films have been fabricated via a facile and scalable CVD method.
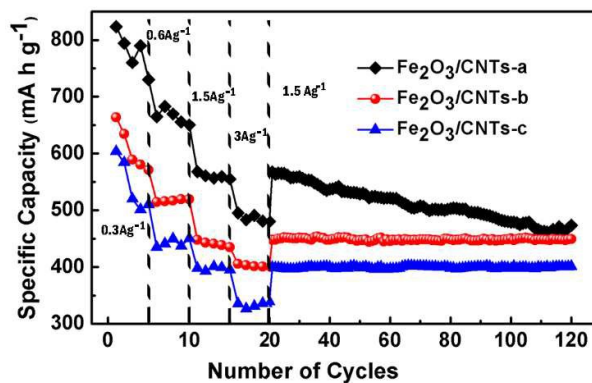

Figure 12. Rate performances and cycling performances of Fe_2O_3/CNTs electrodes with different thicknesses.

Compared to pure Fe_2O_3 NPs and Fe_2O_3/CNTs-mixed, Fe_2O_3-NPs/CNTs composite films delivered a higher initial reversible capacity of 985.8 mA h g^{-1} at current density of 30 mA g^{-1}, and exhibited good rate capability with a capacity retention of 392.4 mA h g^{-1} even at a current density up to 3 A g^{-1}. Meanwhile, the Fe_2O_3-NPs/CNTs composite films showed better cycling performance with a reversible capacity of 375.5 mA h g^{-1} after 800 cycles at the current density of 3 A g^{-1}. The excellent electrochemical performance of Fe_2O_3-NPs/CNTs composite films is ascribed to the increased electrical conductivity and mechanical stability of as-synthesized composite endowed by continuous CNTs network, as well as that low dimensional Fe_2O_3 NPs (5-10 nm) can accommodate the volume change and shorten the route for lithium diffusion. Taken together, these properties are a harbinger of important advances in the next generation higher energy density LIBs. Furthermore, the Fe_2O_3-NPs/CNTs composite films are foldable and can be freely tailored and directly used as electrodes in LIBs. These features make Fe_2O_3-NPs/CNTs films applicable for different electronic devices with various shapes and functions (e.g., portable electronics, smart garments).

Acknowledgements

Notes and references

1   J. B. Goodenough and Y. Kim, *Journal of Power Sources*, 2011, 196, 6688-6694.
2   T.-H. Kim, J.-S. Park, S. K. Chang, S. Choi, J. H. Ryu and H.-K. Song, *Advanced Energy Materials*, 2012, 2, 860-872.
3   J. Cabana, L. Monconduit, D. Larcher and M. R. Palacín, *Advanced Materials*, 2010, 22, E170-E192.
4   P. Poizot, S. Laruelle, S. Grugeon, L. Dupont and J. M. Tarascon, *Nature*, 2000, 407, 496-499.
5   P. Wang, M. X. Gao, H. G. Pan, J. L. Zhang, C. Liang, J. H. Wang, P. Zhou and Y. F. Liu, *Journal of Power Sources*, 2013, 239, 466-474.

6   M. V. Reddy, T. Yu, C.-H. Sow, Z. X. Shen, C. T. Lim, G. V. S. Rao and B. V. R. Chowdari, *Advanced Functional Materials*, 2007, 17, 2792-2799.

7   H. B. Wu, J. S. Chen, H. H. Hng and X. Wen Lou, *Nanoscale*, 2012, 4, 2526-2542.

8   X. Yao, C. Tang, G. Yuan, P. Cui, X. Xu and Z. Liu, *Electrochemistry Communications*, 2011, 13, 1439-1442.

9   P. L. Taberna, S. Mitra, P. Poizot, P. Simon and J. M. Tarascon, *Nature materials*, 2006, 5, 567-573.

10 A. S. Arico, P. Bruce, B. Scrosati, J. M. Tarascon and W. Van Schalkwijk, *Nature Materials*, 2005, 4, 366-377.

11 Y.-G. Guo, J.-S. Hu and L.-J. Wan, *Advanced Materials*, 2008, 20, 2878-2887.

12 N. Kang, J. H. Park, J. Choi, J. Jin, J. Chun, I. G. Jung, J. Jeong, J.-G. Park, S. M. Lee, H. J. Kim and S. U. Son, *Angewandte Chemie-International Edition*, 2012, 51, 6626-6630.

13 C. Wu, Q. C. Zhuang, L. L. Tian, Y. L. Cui and X. X. Zhang, *Materials Letters*, 2013, 107, 27-30.

14 S. Chen, Y. Xin, Y. Zhou, F. Zhang, Y. Ma, H. Zhou and L. Qi, *Journal of Materials Chemistry A*, 2015, 3, 13377-13383.

15 J. Chen, L. N. Xu, W. Y. Li and X. L. Gou, *Advanced Materials*, 2005, 17, 582-+.

16 J. Xin, C. Jia-jia, X. Jian-hui, F. Yi-ning, F. You-zuo, Z. Min-sen and D. Quan-feng, *Chemical communications (Cambridge, England)*, 2012, 48, 7410-7412.

17 Y. Yang, X. Fan, G. Casillas, Z. Peng, G. Ruan, G. Wang, M. J. Yacaman and J. M. Tour, *Acs Nano*, 2014, 8, 3939-3946.

18 Y. Wu, Y. Wei, J. Wang, K. Jiang and S. Fan, *Nano Letters*, 2013, 13, 818-823.

19 Y. Zhao, X. Li, B. Yan, D. Li, S. Lawes and X. Sun, *Journal of Power Sources*, 2015, 274, 869-884.

20 M. Du, C. H. Xu, J. Sun and L. Gao, *Journal of Materials Chemistry A*, 2013, 1, 7154-7158.

21 L. Xiao, M. Schroeder, S. Kluge, A. Balducci, U. Hagemann, C. Schulzad and H. Wiggers, *Journal of Materials Chemistry A*, 2015, 3, 11566-11574.

22 J. Shao, J. X. Zhang, J. J. Jiang, G. M. Zhou and M. Z. Qu, *Electrochimica Acta*, 2011, 56, 7005-7011.

23 Z. Y. Xia, D. Wei, E. Anitowska, V. Bellani, L. Ortolani, V. Morandi, M. Gazzano, A. Zanelli, S. Borini and V. Palermo, *Carbon*, 2015, 84, 254-262.

24 H. X. Gao, F. Hou, Z. P. Wa, S. Zhao, D. M. Yang, J. C. Liu, A. R. Guo and Y. X. Gong, *Electrochimica Acta*, 2015, 154, 321-328.

25 H. X. Gao, F. Hou, X. R. Zheng, J. C. Liu, A. R. Guo, D. M. Yang and Y. X. Gong, *Vacuum*, 2015, 112, 1-4.

26 Q. Guo, P. Guo, J. Li, H. Yin, J. Liu, F. Xiao, D. Shen and N. Li, *Journal of Solid State Chemistry*, 2014, 213, 104-109.

27 M. Wu, J. Chen, C. Wang, F. Wang, B. Yi, W. Su, Z. Wei and S. Liu, *Electrochimica Acta*, 2014, 132, 533-537.

28 S. Chaisitsak, J. Nukeaw and A. Tuantranont, *Diamond and Related Materials*, 2007, 16, 1958-1966.

29 N. Van Quy, Y. S. Cho, G. S. Choi, I. K. Song, W. J. Yu and D. J. Kim, *Nanotechnology*, 2005, 16, 386-390.

30 H. Q. Hou, A. K. Schaper, F. Weller and A. Greiner, *Chemistry of Materials*, 2002, 14, 3990-3994.

31 C. Singh, M. S. Shaffer and A. H. Windle, *Carbon*, 2003, 41, 359-368.

32 V. V. Kovalevski and A. N. Safronov, *Carbon*, 1998, 36, 963-968.

33 S. Q. Chen, P. Bao and G. X. Wan, *Nano Energy*, 2013, 2, 425-434.

34 Y. Z. Piao, H. S. Kim, Y. E. Sung and T. Hyeon, *Chemical Communications*, 2010, 46, 118-120.

35 Z. C. Yang, J. G. Shen, N. Jayaprakash and L. A. Archer, *Energy & Environmental Science*, 2012, 5, 7025-7032.

36 L. W. Ji, O. Toprakci, M. Alcoutlabi, Y. F. Yao, Y. Li, S. Zhang, B. K. Guo, Z. Lin and X. W. Zhang, *Acs Applied Materials & Interfaces*, 2012, 4, 2672-2679.

37 X. Zhu, X. Y. Song, X. L. Ma and G. Q. Ning, *Acs Applied Materials & Interfaces*, 2014, 6, 7189-7197.

38 S. Q. Chen and Y. Wang, *Journal of Materials Chemistry*, 2010, 20, 9735-9739.

39 B. Sun, J. Horvat, H. S. Kim, W.-S. Kim, J. Ahn and G. Wang, *Journal of Physical Chemistry C*, 2010, 114, 18753-18761.

40 S. Laruelle, S. Grugeon, P. Poizot, M. Dolle, L. Dupont and J. M. Tarascon, *Journal of the Electrochemical Society*, 2002, 149, A627-A634.

41 S. W. Kim, D. H. Seo, H. Gwon, J. Kim and K. Kang, *Advanced Materials*, 2010, 22, 5260-5264.

42 C. M. Ban, Z. C. Wu, D. T. Gillaspie, L. Chen, Y. F. Yan, J. L. Blackburn and A. C. Dillon, *Advanced Materials*, 2010, 22, E145-+.

43 S. Goriparti, E. Miele, F. De Angelis, E. Di Fabrizio, R. P. Zaccaria and C. Capiglia, *Journal of Power Sources*, 2014, 257, 421-443.

44 L. Zhang, H. B. Wu and X. W. Lou, *Advanced Energy Materials*, 2014, 4.

45 N. Ogihara, S. Kawauchi, C. Okuda, Y. Itou, Y. Takeuchi and Y. Ukyo, *Journal of the Electrochemical Society*, 2012, 159, A1034-A1039.

46 X. Li, J. Liu, Y. Zhang, Y. Li, H. Liu, X. Meng, J. Yang, D. Geng, D. Wang, D. Wang, R. Li and X. Sun, *Journal of Power Sources*, 2012, 197, 238-245.

47 X. Li, J. Yang, Y. Hu, J. Wang, Y. Li, M. Cai, R. Li and X. Sun, *Journal of Materials Chemistry*, 2012, 22, 18847-18853.

48 H. Zhang, G. P. Cao, Z. Y. Wang, Y. S. Yang, Z. J. Shi and Z. A. Gu, *Electrochimica Acta*, 2010, 55, 2873-2877.

49 Y. Z. Wan, Z. W. Yang, G. Y. Xiong and H. L. Luo, *Journal of Materials Chemistry A*, 2015, 3, 15386-15393.